European Journal of Pharmaceutics and Biopharmaceutics 76 (2010) 17–23

Contents lists available at ScienceDirect

European Journal of Pharmaceutics and Biopharmaceutics

journal homepage: www.elsevier.com/locate/ejpb

Research paper

Inclusion of telmisartan in mesocellular foam nanoparticles: Drug loading and release property

Yanzhuo Zhang [a], Tongying Jiang [a], Qiang Zhang [b], Siling Wang [a,*]

[a] Department of Pharmaceutics, Shenyang Pharmaceutical University, Shenyang, PR China
[b] Department of Pharmaceutics, Peking University, Beijing, PR China

ARTICLE INFO

Article history:
Received 4 March 2010
Accepted in revised form 28 May 2010
Available online 2 June 2010

Keywords:
Drug delivery system
Mesocellular foam
Water-insoluble drugs
Telmisartan
Drug loading
Enhanced dissolution

ABSTRACT

Spherical mesocellular foam (MCF) with a continuous 3-D pore system was synthesized using Pluronic 123 triblock polymer (P123) as a surfactant coupled with cetyltrimethyl ammonium bromide (CTAB) as a co-surfactant. The feasibility of the prepared MCF nanoparticles for oral drug delivery was studied. A model drug, telmisartan (TEL), was loaded onto MCF via a procedure involving a combination of adsorption equilibrium and solvent evaporation. The drug-release rate and the drug loading efficiency of spherical MCF were compared with those of fibrous SBA-15. Investigations using nitrogen adsorption, scanning electron microscopy (SEM), transmission electron microscopy (TEM), wide-angle X-ray scattering (WXRS), differential scanning calorimetry (DSC) and HPLC demonstrated the successful incorporation of TEL into the MCF host. It is found that spherical MCF has a high drug loading efficiency up to 42.9% (drug weight/total weight) and higher than that of SBA-15 with a pore diameter of 6.5 nm. It is shown that a fast release rate of TEL was obtained from MCF compared with SBA-15 and pure crystalline TEL using enzyme-free simulated gastric fluid (pH 1.2) and intestinal fluid (pH 6.8). We believe that the present study will help in the design of oral drug delivery systems for the dissolution enhancement of water-insoluble drugs.

1. Introduction

The oral delivery route is commonly recognized as the most preferred and convenient route for the administration of drug formulations. In order for a drug to be absorbed into the systemic circulation following oral administration, it must be dissolved in gastrointestinal fluids. For hydrophobic drugs belonging to Class II of the Biopharmaceutical Classification System (BCS), it is this dissolution process which acts as the rate-controlling step and, therefore, determines the rate and degree of absorption [1,2]. Consequently, many hydrophobic drugs show incomplete absorption from the gastrointestinal tract. Thus, one of the major current challenges of the pharmaceutical industry involves strategies that improve the water solubility of drugs, since it is estimated that 40% of new chemical entities (NCE) are poorly soluble or insoluble in water [3–7].

In the past decade, silica-based ordered mesoporous materials (OMS) have found widespread application as controlled drug delivery systems (DDS) [8–12]. OMS offer several attractive features for controlled release, such as a high adsorption capacity [13–16]; the homogeneity of the drug distribution in the host is achieved by the well-ordered pore arrangement [15–21], and it is easy to modify the pore dimensions to control the drug delivery kinetics [15,22]. In addition to the pore channels of OMS being able to change the crystalline state of a drug to an amorphous one, the pore channels also restrict drug recrystallization and reduce the particle size of the amorphous drug [10,23]. So far, the most often used OMS-based drug carrier has been the MCM series and the SBA series. Typically, the pore diameter varies between 2 and 6 nm for MCM-41 and between 4 and 13 nm for SBA-15 [22–26]. However, the focus of OMS has been mainly on the development of slow-release formulations, and fewer reports have been published on the application of synthetic OMS involving the dissolution enhancement of water-insoluble drugs [22,27–33]. The mainly reasons for this involve the pore size and geometry of the pore network [10,25]. At first, the pore size is an important factor affecting the drug-release rate. It was found that reducing the pore size could delay the release of a drug [33]. In addition, the majority of OMS exhibit sterical diffusion hindrance caused by the 2-D hexagonally ordered long pore channel as far

Abbreviations: MCF, Mesocellular foam; TEL, telmisartan; TEL–MCF_1, the mass ratio of MCF:TEL was 5:4 in the drug loading procedure; TEL–MCF_2, the mass ratio of MCF:TEL was 1:1 in the drug loading procedure; MCF_a, unloaded MCF; MCF_b, TEL–MCF after complete release of TEL.

* Corresponding author. Address: Shenyang Pharmaceutical University, P.O. Box 32, 103 Wenhua Road, Shenhe District, Shenyang, Liaoning Province 110016, PR China. Tel./fax: +86 24 23986348.
E-mail address: silingwang310@sina.com (S. Wang).

0939-6411/$ - see front matter © 2010 Elsevier B.V. All rights reserved.
doi:10.1016/j.ejpb.2010.05.010

as the loading and diffusion of drugs is concerned. For example, the length of unidirectional pore channels varies between 1 and 20 μm for SBA-15 [26,34]. To overcome these problems, it is essential to develop a novel drug-loaded OMS in a way that allows an enhanced dissolution rate. MCF composed of uniformly sized, large spherical cells that are interconnected by uniform windows to create a continuous 3-D pore system [35,36]. The interconnected nature of the large uniform pores makes this mesostructured silica promising candidate for drug delivery device with fast release property.

In the current study, we synthesized spherical MCF with a continuous 3-D pore system using P123 as a surfactant coupled with CTAB as a co-surfactant and, to the best of our knowledge, the pharmaceutical performance of this material has not been documented so far. The advantages of the large pore size and ordered 3-D pore system allowed easy accessibility as well as fast release characteristics for the uptake and release of the study drug. The effects of the large pore size and ordered 3-D pore system of MCF on the uptake and release of the model drug TEL (Fig. 1) were systematically studied using nitrogen adsorption, scanning electron microscopy (SEM), transmission electron microscopy (TEM), wide-angle X-ray scattering (WXRS), differential scanning calorimetry (DSC) and HPLC.

2. Materials and methods

2.1. Materials

Guaranteed-grade cetyltrimethyl ammonium bromide (CTAB), 1,3,5-trimethylbenzene (TMB), tetraethyl orthosilicate (TEOS), ammonia tetrafluoride, HPLC-grade methanol, potassium dihydrogen phosphate, hydrochloric acid, acetic acid and sodium hydroxide were purchased from Aladdin (Shanghai, China). Pluronic 123 triblock polymer (P123) [$(EO)_{20}(PO)_{70}(EO)_{20}$, molecular weight, MW = 5800] and TEL (purity ⩾ 98%) were purchased from Sigma–Aldrich (St. Louis, MO, USA). All other chemicals were of reagent grade and were used as purchased without further purification. Deionized water was prepared by ion exchange.

2.2. Synthesis of spherical MCF nanoparticles

Spherical MCF nanoparticles were synthesized in aqueous hydrochloric acid using P123 as a structure-directing agent and TMB as a micelle expander. In a typical synthesis, 2.4 g P123 was dissolved in 90 ml of 1.6 M hydrochloric acid solution at room temperature. Subsequently, 0.4 g CTAB, 0.025 g ammonia tetrafluoride and 1.6 ml TMB were added to the surfactant solution, and the mixture was stirred for 2 h. A volume of 5.5 ml TEOS was added drop by drop to the surfactant solution under vigorous stirring. The stirring was allowed to continue for another 5 min before switching to static synthesis conditions at 38 °C. After 20 h, the milky reaction mixture was transferred to a Teflon-lined autoclave and crystallized for another 24 h at 120 °C. As-synthesized material was filtered, washed with ethanol and dried at 60 °C in a vacuum oven. Finally, the resulting powder was calcined in air at 600 °C for 5 h at a heating rate of 2 °C min^{-1} to remove the organic template.

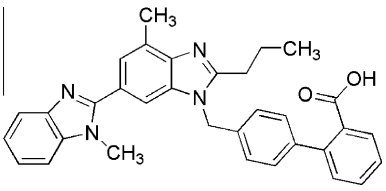

Fig. 1. Molecular structure of Telmisartan.

Fibrous SBA-15 microparticles were synthesized according to the procedure reported by Zhao et al. with some modifications [18]. Briefly, 2.0 g P123 was dissolved in a mixture of 15 ml water and 60 ml 2 M hydrochloric acid solution with constant stirring at 38 °C then, after 1 h, 4.6 ml TEOS was added to this solution. Following this, the reaction solution was stirred for 24 h at 38 °C, and the mixed solution was then crystallized at 90 °C for 24 h. The solid product was filtered, washed with ethanol, dried in air and calcined at 600 °C for 5 h.

2.3. TEL-loading procedure

TEL, a well-known anti-hypertensive drug, was selected as a model drug due to its very poor intestinal solubility, which depended on the pH of the medium as a BCS class II drug with an aqueous solubility of 0.09 μg/ml and a p*K*a of 4.45 ± 0.09 [37]. A drug loading procedure involving a combination of adsorption equilibrium and solvent evaporation was developed in order to enhance the drug loading efficiency. Briefly, TEL adsorption into MCF was carried out by soaking the MCF nanoparticles in an acetic acid solution of TEL (60 mg/ml). The carrier:drug ratio in the loading solution was varied from 5:1 to 1:1 (w:w). Then, the mixture was ultrasonicated for a few minutes and brought to adsorption equilibrium under gentle vortexing for 12 h in order to achieve maximum loading in the pore channels of the MCF nanoparticles. The loading was performed under ambient conditions (about 20 °C) in closed containers to prevent evaporation of acetic acid during the loading period. Finally, the mixture was dried at 55 °C under vacuum for 24 h. The drug-loaded sample was referred to as TEL–MCF. The procedure for TEL loading into the SBA-15 microparticles was similar to that used for load MCF. The dried drug-loaded sample was referred to as TEL–SBA-15.

2.4. SEM and TEM studies

The morphology and particle size of the prepared samples were characterized using a JSM-6301F SEM instrument (JEOL, Japan) operated at 15 kV. The samples were gold-plated prior to imaging. The porous structure of the samples was characterized using a Tecnai G^2 F30 TEM instrument (FEI, The Netherlands) operated at 200 kV. Before examination, the samples were dispersed in deionized water through sonication and subsequently deposited on carbon-coated copper grids.

2.5. Nitrogen adsorption analysis

The pore characteristics of the samples were studied by determining the nitrogen adsorption using a SA3100 surface area and pore size analyzer (Beckman Coulter, USA) at −196 °C [20]. The specific surface area, S_{BET}, was evaluated from nitrogen adsorption data over the relative pressure range from 0.05 to 0.2 using the Brunauer–Emmett–Teller (BET) method. The total pore volume, V_t, was determined from the amount adsorbed at a relative pressure of 0.99. Pore size distributions (PSDs) were determined from adsorption branches of isotherms using the Barrett–Joyner–Halenda (BJH) method with the Kelvin equation for a hemispherical meniscus and the statistical film thickness curve for macroporous silica. The BJH pore diameter, w_{BJH}, is defined as a position of the maximum on the pore size distribution curve. The MCF (or SBA-15) samples were degassed at 300 °C for 12 h prior to analysis, while the TEL-loaded samples were degassed at 50 °C for 12 h. The experiments were performed in triplicate.

2.6. WAXS and DSC studies

WAXS was used for the identification of the crystals (structure and changes) of the TEL-loaded samples and also the pure TEL. WAXS patterns of the prepared samples were obtained using an X'pert PRO diffractometer (PANalytical B.V., The Netherlands), with an Ni filtered Cu–Ka line as the source of radiation, and the equipment was operated at a voltage of 40 kV and a current of 30 mA. All samples were measured over the 2θ angle range from 5° to 35° with a scan rate of 4°/min and a step size of 0.02°. The physical state of the pure TEL and the TEL-loaded samples was also examined by DSC. The thermographs of each powder were obtained using a Q1000 DSC instrument (TA Instruments, USA). The TEL-loaded samples equivalent to 4 mg TEL and pure TEL (4 mg) were placed in pierced aluminum pans and heated from 50 to 300 °C at a scanning rate of 10 °C min^{-1} in a nitrogen atmosphere.

2.7. HPLC analysis and the drug loading efficiency

TEL was analyzed using a Hitachi™ HPLC system consisting of an L7100 pump and an L7420 UV–VIS tunable absorbance detector (Japan). Analysis was carried out on a Shim-pack C_{18} column (250 × 4.6 mm, 5 μm). The mobile phase consisted of an 80:20 (% v/v) mixture of methanol and 5 mM potassium dihydrogen phosphate solution, and the flow rate was 1.0 ml/min, and the detection wavelength was 296 nm. The injection volume was 10 μl. The sample was passed through a 0.22-μm polytetrafluoroethylene (PTFE) membrane filter before the HPLC analysis. The standard curves were linear over the concentration range of 0.5–10 μg/ml. The drug loading was determined by extracting 10 mg of the TEL-loaded samples with 200 ml methanol for 12 h with stirring, followed by filtration of the sample and analysis by HPLC [23,27]. The experiments were performed in triplicate.

2.8. In vitro drug-release study

In vitro drug-release study was conducted using a USP II paddle method (50 rpm, 37 °C and 900 ml dissolution medium) with a D-800 LS dissolution tester (Tianjin University Radio Factory, China). The TEL-loaded samples equivalent to 40 mg TEL were exposed for 6 h to two different media: enzyme-free simulated gastric fluid (pH 1.2) prepared by adding 2.0 g sodium chloride, 7.0 ml hydrochloric acid and sufficient deionized water to make 1 L enzyme-free simulated gastric fluid and enzyme-free simulated intestinal fluid (pH 6.8) prepared by adding 6.8 g potassium dihydrogen phosphate in deionized water and adjusting the pH with 1 M sodium hydroxide solution to make 1 L enzyme-free simulated intestinal fluid [37]. At predetermined time intervals, 5 ml samples were withdrawn and immediately replaced with an equal volume of dissolution medium to keep the volume constant. The withdrawn samples were filtered, suitably diluted, and then, the drug concentration was determined by HPLC. All data were reported as the mean ± standard deviation (SD). Statistical analysis was performed for the experiments conducted in triplicate using Student's *t*-test. Results with $p < 0.05$ were considered to be statistically significant.

3. Results and discussion

3.1. Morphology and particle size of the prepared nanoparticles

SEM imaging showed that the prepared MCF sample consisted of many spherical particles with relatively uniform sizes of about 800 nm in diameter (Fig. 2a). The TEM micrograph of MCF nanoparticles also revealed that these have spherical shape, with dimensions similar to those found through SEM measurements (Fig. 2b). Examination of these nanoparticles at higher magnifications shows that they have a porous structure (Fig. 2c). MCF composed of uniformly sized, large spherical cells that are interconnected by uniform windows to create a continuous 3-D pore system. In addition, the TEM image of TEL–MCF clearly shows that the ordered 3-D pore structures were still present in the TEL-loaded samples (Fig. 2d).

SEM imaging showed that the SBA-15 sample consisted of many rod-like sub-particles with relatively uniform sizes of about 0.5 μm in diameter and 1–2 μm in length, which are aggregated into wheat-like macrostructures (Fig. 3a). Similar SEM images were reported by Katiyar et al. [34]. As shown in Fig. 3b, the TEM micrograph of SBA-15 was recorded with the electron beam direction nearly parallel to the channel direction. The TEM image confirms the ordered structure of SBA-15 and shows that the cylindrical pores are arranged in an ordered array.

3.2. Nitrogen adsorption analysis

The nitrogen adsorption/desorption isotherms of the prepared MCF samples were typical type IV isotherms according to the IUPAC classification, characteristic of mesoporous materials [20,35]. As an example, the nitrogen adsorption/desorption isotherms of MCF_a (unloaded MCF), TEL–MCF (the mass ratio of MCF:TEL was 5:4 in the drug loading procedure) and MCF_b (TEL–MCF after complete release of TEL) are presented in Fig. 4A, and the nitrogen adsorption/desorption isotherms of SBA-15_a (unloaded SBA-15), TEL–SBA-15 (the mass ratio of SBA-15:TEL was 5:3 in the drug loading procedure) and SBA-15_b (TEL–SBA-15 after complete release of TEL) are presented in Fig. 4B. The isotherms of MCF (or SBA-15) featured hysteresis loops with sharp adsorption and desorption branches. The pore size distributions of the prepared samples are presented in Fig. 5. The values for the BET specific surface area (S_{BET}), the total pore volume (V_t) and the BJH pore diameter (w_{BJH}) are given in Table 1. It can be seen that the MCF (or SBA-15) samples possess high S_{BET} and V_t, indicating its potential application as a host for bonding or storing more drug molecules in the drug storage/release system. Furthermore, S_{BET}, V_t and w_{BJH} were reduced apparently after TEL has been loaded, confirming that TEL was incorporated into MCF (or SBA-15) pore channels. Finally, it is worthwhile to point out that MCF (or SBA-15) still exhibits typical IV isotherms after complete release of TEL, and S_{BET}, V_t and w_{BJH} can almost be recovered, indicating the good stability of this drug-release system.

3.3. Physicochemical characterization

The WAXS patterns of the drug-loaded samples were recorded to determine whether a crystalline drug phase would be detected [24,25]. The WAXS patterns of TEL, MCF, physical mixture and TEL–MCF are given in Fig. 6. The diffraction pattern of pure TEL was highly crystalline in nature as indicated by numerous peaks. The main peaks at 6.7° and 14.1° were particularly distinctive. For the physical mixture of TEL and MCF, peaks at 6.7° and 14.1° were attributed to pure TEL. However, no crystalline TEL was detected in the TEL–MCF_1 samples (Fig. 6e, the mass ratio of MCF:TEL was 5:4 in the drug loading procedure). In contrast, TEL peaks of the TEL–MCF_2 samples were observed (Fig. 6d, the mass ratio of MCF:TEL was 1:1 in the drug loading procedure). It was found that the prepared MCF nanoparticles have a high drug loading efficiency up to 42.9% (drug weight/total weight). On the other hand, no crystalline TEL was detected in the TEL–SBA-15_1 samples (Fig. 7e, the mass ratio of SBA-15:TEL was 5:3 in the drug loading procedure). In contrast, TEL peaks of the TEL–SBA-15_2 samples were observed (Fig. 7d, the mass ratio of SBA-15:TEL was 5:4 in the drug loading procedure). It was found that the maximum drug loading efficiency of the prepared SBA-15 microparticles was

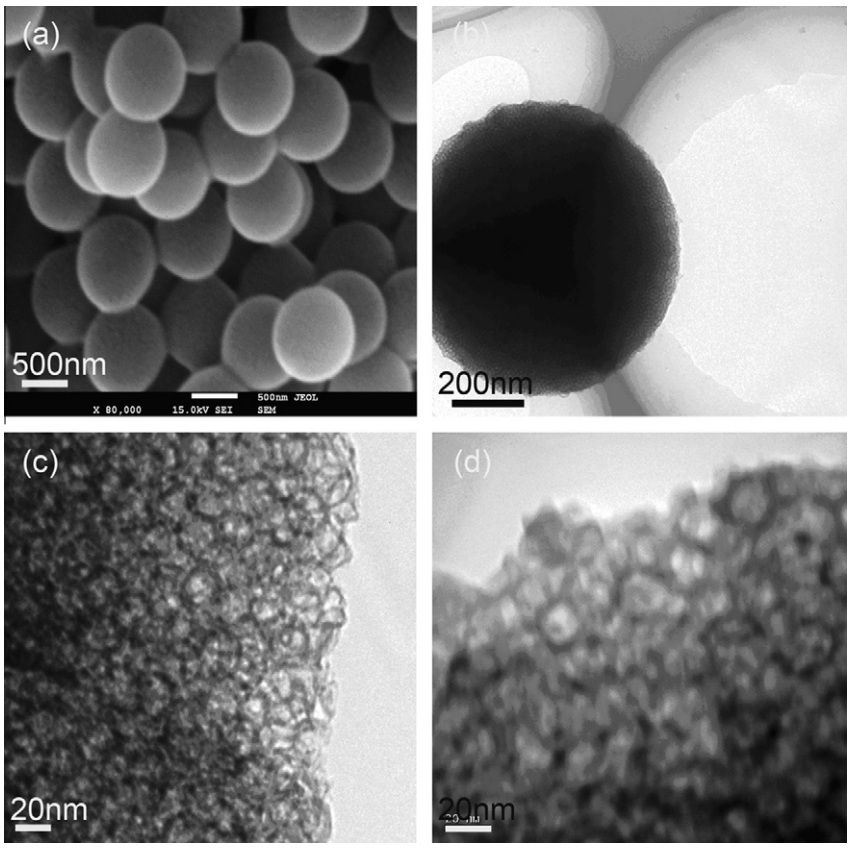

Fig. 2. SEM photograph of (a) MCF; TEM photographs of (b) MCF, (c) MCF (enlarge) and (d) TEL–MCF.

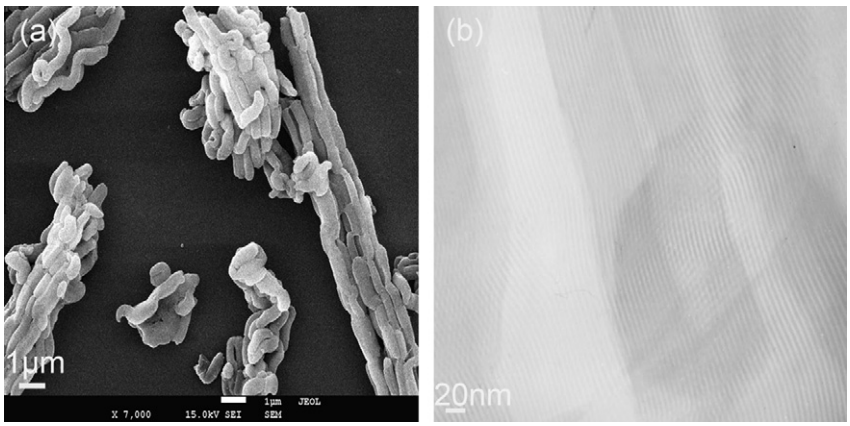

Fig. 3. (a) SEM photograph and (b) TEM photograph of SBA-15.

approximately 37.1%. In agreement with previous reports, the drug loading capacity of an OMS was very dependent on its S_{BET} and V_t. The relatively high S_{BET} and V_t of an OMS enabled it to achieve a high drug loading efficiency [15,27]. However, there were some differences in the maximum drug loading efficiency of the prepared particles, the MCF samples (V_t was 1.73 cm^3/g) exhibited a higher drug loading efficiency than the SBA-15 samples (V_t was 1.21 cm^3/g), while the S_{BET} of MCF was less than SBA-15.

The presence or absence of crystalline drug was also confirmed by DSC analysis using the drug melting peak in the thermograms as an indication that TEL in crystalline form was present in the sample. If the drug in the pores is in a crystalline state, the amount of drug can be estimated from the melting point depression using DSC. If the drug in the pores is in a noncrystalline state, no melting point depression can be detected [22–24]. Thermograms of TEL–MCF were recorded, and signals due to melting could be observed. As an example, the DSC curves for TEL, MCF and TEL–MCF are presented in Fig. 8. DSC analysis of crystalline TEL showed a single sharp endothermic peak at 272.5 °C, which corresponded to its intrinsic melting point (the endothermic value was 102.6 J/g). No characteristic melting peak of TEL was identified in the DSC curve obtained from TEL–MCF_1 (Fig. 8c). The absence of phase transitions owing to TEL in the DSC analysis is evidence that TEL is in an amorphous state. In contrast, the melting peak of TEL can be observed at 270.1 °C in the DSC curve obtained from TEL–MCF_2 (Fig. 8b, the endothermic value was 7.9 J/g, while the endothermic value of equivalent pure TEL was 102.6 J/g), which confirms the results obtained from the WAXS study.

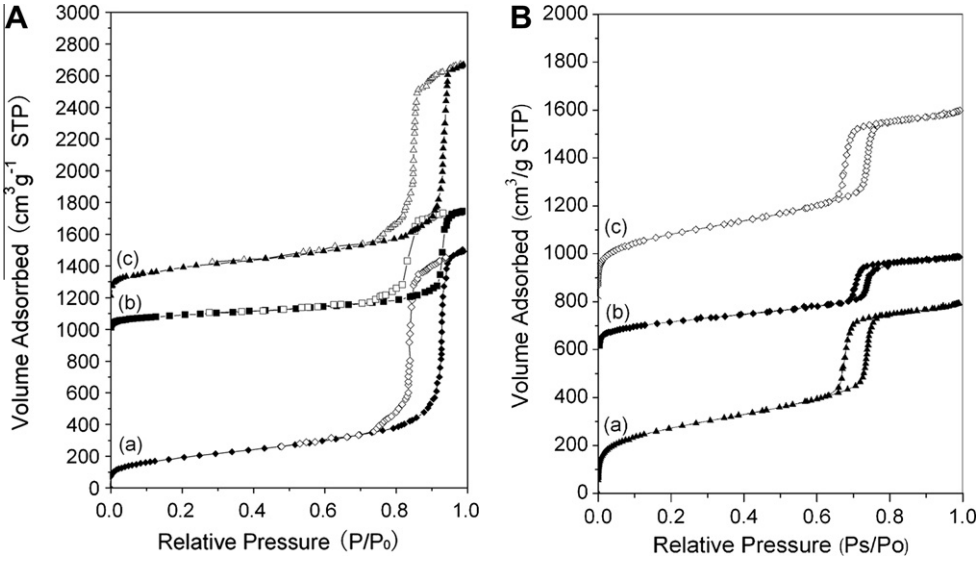

Fig. 4. (A) Nitrogen adsorption/desorption isotherms of (a) MCF_a, (b) TEL–MCF and (c) MCF_b. The isotherms of (b) and (c) were offset vertically by 1000 and 1200 (cm^3/g STP), respectively. (B) Nitrogen adsorption/desorption isotherms of (a) SBA-15_a, (b) TEL–SBA-15 and (c) SBA-15_b. The isotherms of (b) and (c) were offset vertically by 600 and 800 (cm^3/g STP), respectively.

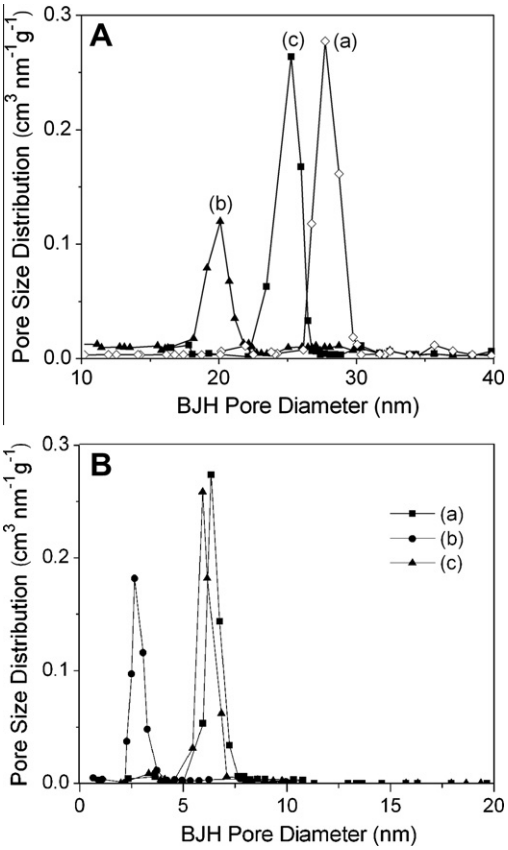

Fig. 5. (A) Pore size distributions of (a) MCF_a, (b) TEL–MCF and (c) MCF_b. (B) Pore size distributions of (a) SBA-15_a, (b) TEL–SBA-15 and (c) SBA-15_b.

3.4. In vitro drug-release study

The effects of different pore sizes and pore structures on the TEL release rate in enzyme-free simulated gastric fluid (pH 1.2) and intestinal fluid (pH 6.8) are shown in Figs. 9 and 10, respectively. Under the low pH of the dissolution experiment, TEL is highly soluble on its own [37], thus the dissolution improvement offered by the carriers is not expected to be as significant. The dissolution rate of TEL released from TEL-loaded SBA-15 samples was slower compared with the dissolution rate of pure TEL and TEL-loaded MCF samples due to SBA-15 retarding sterical diffusion caused by the long and tight pore channels and the ordered 2-D cylindrical pore systems. Since the solubility of TEL is dependent on the pH and is high under strongly acidic or basic conditions (the solubility of crystalline TEL was 552.37 ± 10.91 μg/ml in enzyme-free simulated gastric fluid), but very low under neutral conditions (the solubility of crystalline TEL was 0.34 ± 0.07 μg/ml in enzyme-free simulated intestinal fluid), the observed dissolution rate of the

Table 1
Structural properties of the samples (n = 3).

Sample	S_{BET} (m^2/g)	V_t (cm^3/g)	w_{BJH} (nm)	Drug loading (%)
MCF_a	816.0 ± 7.2	1.73 ± 0.04	28.3 ± 2.4	–
TEL–MCF	190.3 ± 14.1	0.60 ± 0.11	20.1 ± 3.3	42.9 ± 3.1
MCF_b	795.2 ± 16.7	1.59 ± 0.06	26.0 ± 3.9	–
SBA-15_a	982.4 ± 5.6	1.21 ± 0.03	6.5 ± 1.7	–
TEL–SBA-15	210.3 ± 24.9	0.45 ± 0.08	2.8 ± 1.2	37.1 ± 2.5
SBA-15_b	977.5 ± 12.6	1.14 ± 0.05	6.3 ± 2.0	

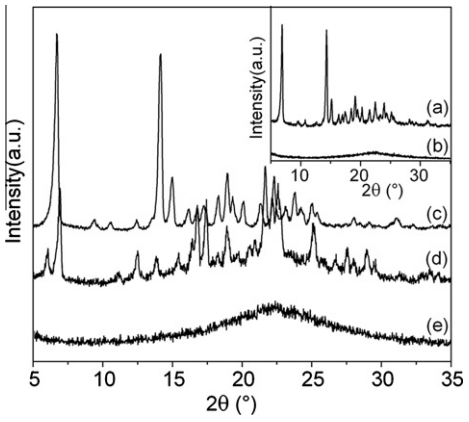

Fig. 6. WAXS patterns of (a) TEL, (b) MCF, (c) physical mixture, (d) TEL–MCF_2 and (e) TEL–MCF_1.

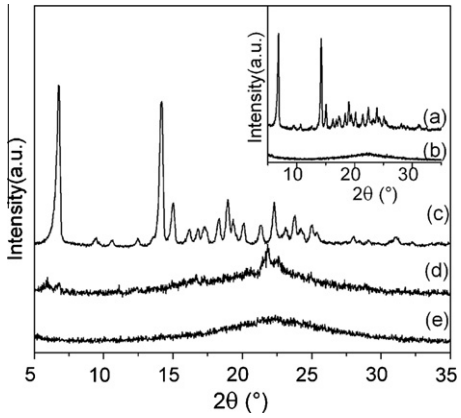

Fig. 7. WAXS patterns of (a) TEL, (b) SBA-15, (c) physical mixture, (d) TEL–SBA-15$_2$ and (e) TEL–SBA-15$_1$.

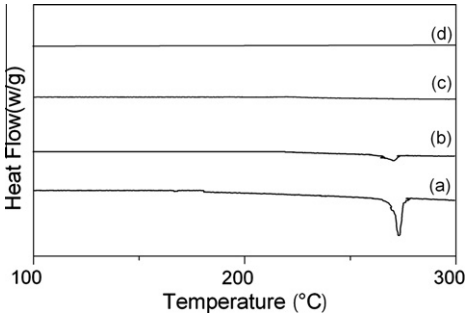

Fig. 8. DSC thermograms of (a) TEL, (b) TEL–MCF$_2$, (c) TEL–MCF$_1$ and (d) MCF.

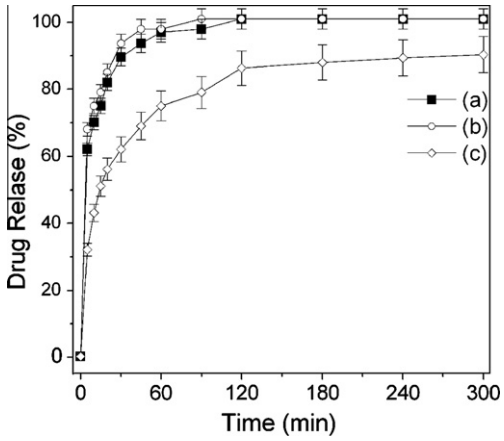

Fig. 9. Dissolution profiles of TEL from (a) pure crystalline TEL, (b) TEL–MCF$_1$ and (c) TEL–SBA-15$_1$ in enzyme-free simulated gastric fluid (pH 1.2). Each data point represents the mean ± SD of three determinations.

pure crystalline TEL was quite low in enzyme-free simulated intestinal fluid (pH 6.8). It is obviously shown that the dissolution rate of TEL loaded from MCF or SBA-15 seems less pH dependent. The amounts of dissolved TEL in the intestinal fluid at sampling times of 10, 20 and 45 min accumulated to 69%, 82% and 94% for TEL–MCF$_1$. The corresponding amounts were 42%, 53% and 65% for TEL–SBA-15$_1$. The dissolution improvement may be largely attributed to the pore channels of the two carriers changing the crystalline state of TEL to an amorphous state (the solubility of amorphous TEL was 49.65 ± 7.22 μg/ml for TEL–MCF$_1$ and 43.21 ± 11.57 μg/ml for TEL–SBA-15$_1$ in enzyme-free simulated intestinal fluid), which is known to improve drug solubility and

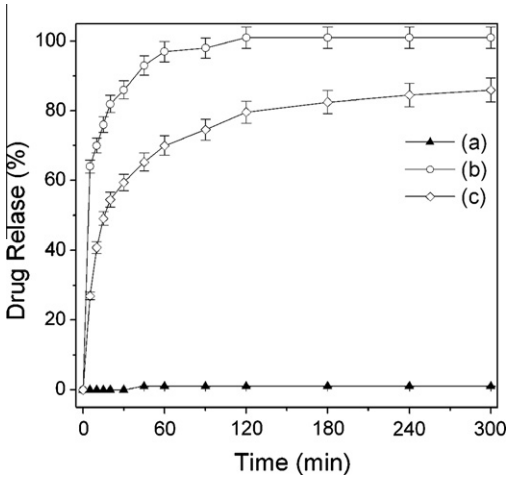

Fig. 10. Dissolution profiles of TEL from (a) pure crystalline TEL, (b) TEL–MCF$_1$ and (c) TEL–SBA-15$_1$ in enzyme-free simulated intestinal fluid (pH 6.8). Each data point represents the mean ± SD of three determinations.

drug dissolution rate. In addition, a high surface area also accelerates the drug-release profile and, consequently, improves the dissolution rate [3,27]. It is obviously shown that the faster TEL release of two TEL-loaded samples was observed from TEL–MCF. The difference in release rate between MCF and SBA-15 could be attributed to the pore sizes and pore structures. It is known that fast drug release could be achieved by enlarging the pore size of mesoporous carrier. Therefore, MCF (w_{BJH} was 28.3 nm) exhibited a lower sterical diffusion hindrance caused by pore channel compared with SBA-15 (w_{BJH} was 6.5 nm). In addition, the TEL molecules adsorbed in the ordered 3-D spherical pore systems (the spherical cells with relatively uniform sizes of about 25 nm in diameter, as shown in Fig. 2c) have a greater chance of escaping from mesopore channels and diffusing into the release medium compared with those adsorbed in the ordered 2-D cylindrical pore systems (the pore channels with relatively uniform sizes of about 6 nm in diameter and 1–2 μm in length, as shown in Fig. 3).

4. Conclusions

The results of this work demonstrated the successful uptake and then release of a model drug in the spherical MCF nanoparticles, confirming for the first time the potential of the spherical MCF nanoparticles as a drug delivery system. MCF with a continuous 3-D pore system has a high drug loading efficiency up to 42.9%. *In vitro* drug-release study show that the dissolution rate of TEL released from MCF was significantly faster compared with crystalline TEL. The dissolution improvement was associated with MCF converting the loaded drug from the solid state to the amorphous form, which typically dissolves faster compared with the crystalline form. In addition, our study shows that the differences in pore size and structure of OMS play an important role in controlling the release rate of drug molecules, with a fast release of TEL from MCF compared with SBA-15. Since drug release is a crucial and limiting step for oral drug absorption, particularly for drugs with low gastrointestinal solubility and high permeability, spherical MCF nanoparticles might offer a larger window of absorption for the drug in the gastrointestinal tract by improving the dissolution rate of water-insoluble drugs.

Acknowledgements

This work was supported by the National Basic Research Program of China (973 Program) (No. 2009CB930300). We would like to thank Dr. David Jack for correcting language.

References

[1] C.A. Lipinski, F. Lombardo, B.W. Dominy, P.J. Feeney, Experimental and computational approaches to estimate solubility and permeability in drug discovery and development setting, Adv. Drug Deliv. Rev. 46 (2001) 3–26.

[2] C.A. Lipinski, Poor aqueous solubility – an industry wide problem in drug discovery, Am. Pharm. Rev. 5 (2002) 82–85.

[3] T. Vasconcelos, B. Sarmento, P. Costa, Solid dispersions as strategy to improve oral bioavailability of poor water soluble drugs, Drug Discov. Today 12 (2007) 1068–1075.

[4] F. Kesisoglou, S. Panmai, Y. Wu, Nanosizing – oral formulation development and biopharmaceutical evaluation, Adv. Drug Deliv. Rev. 59 (2007) 631–644.

[5] K. Sachs-Barrable, S.D. Lee, E.K. Wasan, S.J. Thornton, K.M. Wasan, Enhancing drug absorption using lipids: a case study presenting the development and pharmacological evaluation of a novel lipid-based oral amphotericin B formulation for the treatment of systemic fungal infections, Adv. Drug Deliv. Rev. 60 (2008) 692–701.

[6] S.M. Wong, I.W. Kellaway, S. Murdan, Enhancement of the dissolution rate and oral absorption of a poorly water soluble drug by formation of surfactant-containing microparticles, Int. J. Pharm. 317 (2006) 61–68.

[7] R.N. Gursoy, S. Benita, Self-emulsifying drug delivery systems (SEDDS) for improved oral delivery of lipophilic drug, Biomed. Pharmacother. 58 (2004) 173–182.

[8] C. Barbé, J. Bartlett, L. Kong, K. Finnie, H.Q. Lin, M. Larkin, Silica particles: a novel drug-delivery system, Adv. Mater. 16 (2004) 1949–1966.

[9] M. Vallet-Regi, F. Balas, D. Arcos, Mesoporous materials for drug delivery, Angew. Chem. Int. Ed. 46 (2007) 7548–7558.

[10] S. Wang, Ordered mesoporous materials for drug delivery, Micropor. Mesopor. Mater. 117 (2009) 1–9.

[11] M. Kilpeläinen, J. Riikonen, M.A. Vlasova, A. Huotari, V.P. Lehto, J. Salonen, K.H. Herzig, K. Järvinen, In vivo delivery of a peptide, ghrelin antagonist, with mesoporous silicon microparticles, J. Control. Release 137 (2009) 166–170.

[12] J.H. Park, L. Gu, G. Maltzahn, E. Ruoslahti, S.N. Bhatia, M.J. Sailor, Biodegradable luminescent porous silicon nanoparticles for in vivo applications, Nature Mater. 8 (2009) 331–336.

[13] J.F. Chen, H.M. Ding, J.X. Wang, L. Shao, Preparation and characterization of porous hollow silica nanoparticles for drug delivery application, Biomaterials 25 (2004) 723–727.

[14] C. Charnay, S. Bégu, C. Tourné-Péteilh, L. Nicole, D.A. Lerner, J.M. Devoisselle, Inclusion of ibuprofen in mesoporous templated silica: drug loading and release property, Eur. J. Pharm. Biopharm. 57 (2004) 533–540.

[15] P.P. Yang, Z.W. Quan, L.L. Lu, S.S. Huang, J. Lin, Luminescence functionalization of mesoporous silica with different morphologies and applications as drug delivery systems, Biomaterials 29 (2008) 692–702.

[16] Q.J. He, J.M. Zhang, J.L. Shi, Z.Y. Zhu, L.X. Zhang, W.B. Bu, L.M. Guo, Y. Chen, The effect of PEGylation of mesoporous silica nanoparticles on nonspecific binding of serum proteins and cellular responses, Biomaterials 31 (2010) 1085–1092.

[17] F. Torney, B.G. Trewyn, V.S.Y. Lin, K. Wang, Mesoporous silica nanoparticles deliver DNA and chemicals into plants, Nat. Nanotechnol. 2 (2007) 295–300.

[18] D.Y. Zhao, J.L. Feng, Q.S. Huo, N. Melosh, G.H. Fredrickson, B.F. Chmelka, G.D. Stucky, Triblock copolymer syntheses of mesoporous silica with periodic 50–300 angstrom pores, Science 279 (1998) 548–552.

[19] C.T. Kresge, M.E. Leonowicz, W.J. Roth, J.C. Vartuli, J.S. Beck, Ordered mesoporous molecular sieves synthesized by a liquid-crystal template mechanism, Nature 359 (1992) 710–712.

[20] L. Cao, T. Man, M. Kruk, Synthesis of ultra-large-pore SBA-15 silica with two-dimensional hexagonal structure using triisopropylbenzene as micelle expander, Chem. Mater. 21 (2009) 1144–1153.

[21] C.H. Lee, T.S. Lin, C.Y. Mou, Mesoporous materials for encapsulating enzymes, Nano Today 4 (2009) 165–179.

[22] R. Mellaerts, R. Mols, J.A.G. Jammaer, C.A. Aerts, P. Annaert, J.V. Humbeeck, G.V. Mooter, P. Augustijns, J.A. Martens, Increasing the oral bioavailability of the poorly water soluble drug itraconazole with ordered mesoporous silica, Eur. J. Pharm. Biopharm. 69 (2008) 223–230.

[23] J. Salonen, L. Laitinen, A.M. Kaukonen, J. Tuura, M. Björkqvist, T. Heikkilä, K. Vähä-Heikkilä, J. Hirvonen, V.-P. Lehto, Mesoporous silicon microparticles for oral drug delivery: loading and release of five model drugs, J. Control. Release 108 (2005) 362–374.

[24] H. Yu, Q.Z. Zhai, Mesoporous SBA-15 molecular sieve as a carrier for controlled release of nimodipine, Micropor. Mesopor. Mater. 123 (2009) 298–305.

[25] T. Heikkilä, J. Salonen, J. Tuura, M.S. Hamdy, G. Mul, N. Kumar, T. Salmi, D.Y. Murzin, L. Laitinen, A.M. Kaukonen, J. Hirvonen, V.P. Lehto, Mesoporous silica material TUD-1 as a drug delivery system, Int. J. Pharm. 331 (2007) 133–138.

[26] Y.J. Li, G.W. Zhou, C.J. Li, D.W. Qin, W.T. Qiao, B. Chu, Adsorption and catalytic activity of Porcine pancreatic lipase on rod-like SBA-15 mesoporous material, Colloids Surf. A 341 (2009) 79–85.

[27] M.J.K. Thomas, I. Slipper, A. Walunj, A. Jain, M.E. Favretto, P. Kallinteri, D. Douroumis, Inclusion of poorly soluble drugs in highly ordered mesoporous silica nanoparticles, Int. J. Pharm. 387 (2009) 272–277.

[28] B. Munoz, A. Ramila, J. Pérez-Pariente, I. Diaz, M. Vallet-Regi, MCM-41 organic modification as drug delivery rate regulator, Chem. Mater. 15 (2003) 500–503.

[29] S.W. Song, K. Hidajat, S. Kawi, Functionalized SBA-15 materials as carriers for controlled drug delivery: influence of surface properties on matrix-drug interactions, Langmuir 21 (2005) 9568–9575.

[30] J.C. Doadrio, E.M.B. Sousa, I. Izquierdo-Barba, A.L. Doadrio, J. Pérez-Pariente, M. Vallet-Regi, Functionalization of mesoporous materials with long alkyl chains as a strategy for controlling drug delivery pattern, J. Mater. Chem. 16 (2006) 462–466.

[31] N.K. Mal, M. Fujiwara, Y. Tanaka, Photocontrolled reversible release of guest molecules from coumarin-modified mesoporous silica, Nature 421 (2003) 350–353.

[32] B.G. Trewyn, I.I. Slowing, S. Giri, H.T. Chen, V.S.Y. Lin, Synthesis and functionalization of a mesoporous silica nanoparticle based on the sol–gel process and applications in controlled release, Acc. Chem. Res. 40 (2007) 846–853.

[33] P. Horcajada, A. Rámila, J. Pérez-Pariente, M. Vallet-Regi, Influence of pore size of MCM-41 matrices on drug delivery rate, Micropor. Mesopor. Mater. 68 (2004) 105–109.

[34] A. Katiyar, S. Yadav, P.G. Smirniotis, N.G. Pinto, Synthesis of ordered large pore SBA-15 spherical particles for adsorption of biomolecules, J. Chromatogr. A 1122 (2006) 13–20.

[35] P. Schmidt-Winkel, W.W. Lukens Jr., D. Zhao, P. Yang, B.F. Chmelka, G.D. Stucky, Mesocellular siliceous foams with uniformly sized cells and windows, J. Am. Chem. Soc. 121 (1999) 254–255.

[36] J.S. Lettow, Y.J. Han, P. Schmidt-Winkel, P. Yang, D. Zhao, G.D. Stucky, J.Y. Ying, Hexagonal to mesocellular foam phase transition in polymer-templated mesoporous silicas, Langmuir 16 (2000) 8291–8295.

[37] P.H.L. Tran, H.T.T. Tran, B.J. Lee, Modulation of microenvironmental pH and crystallinity of ionizable telmisartan using alkalizers in solid dispersions for controlled release, J. Control. Release 129 (2008) 59–65.